We are IntechOpen, the world's leading publisher of Open Access books
Built by scientists, for scientists

6,900
Open access books available

185,000
International authors and editors

200M
Downloads

154
Countries delivered to

Our authors are among the

TOP 1%
most cited scientists

12.2%
Contributors from top 500 universities

CLARIVATE ANALYTICS
BOOK CITATION INDEX
INDEXED

WEB OF SCIENCE™

Selection of our books indexed in the Book Citation Index
in Web of Science™ Core Collection (BKCI)

Interested in publishing with us?
Contact book.department@intechopen.com

Numbers displayed above are based on latest data collected.
For more information visit www.intechopen.com

Remote Sensing with Shipborne High-Frequency Surface-Wave Radar

Junhao Xie, Minglei Sun, Zhenyuan Ji and
Guowei Yao

Additional information is available at the end of the chapter

Abstract

High-frequency surface-wave radar (HFSWR) has been successfully applied for moving target detection and remote sensing of ocean surface dynamic parameters for decades. Compared with conventional instruments such as buoys, anemometers, and microwave radars, HFSWR can be employed to an all-weather and all-time surveillance far beyond the visible horizon. Moreover, based on agility and maneuverability, shipborne HFSWR can not only enhance the survivability in complex ocean environment but also enlarge the detection distance on open sea, which will gradually become a popular deployment situation. In this chapter, ocean surface cross sections for shipborne HFSWR with linear platform motion and sway motion are derived theoretically. Then, the methods for ocean surface wind direction, wind field, and current extraction are presented. The computer simulations and experimental results of the real data are given to verify the detection accuracy and the distance limit of the abovementioned methods.

Keywords: shipborne HFSWR (high-frequency surface-wave radar), ocean surface cross section, ocean surface wind field, ocean surface current

1. Introduction

High-frequency surface-wave radar (HFSWR) has been widely applied to early warning for decades, including the detection of airborne targets and surface targets. Its vertically polarized electromagnetic wave (3–30 MHz) follows the curvature of the Earth along the air-water interface and has a very low propagation loss on the ocean surface. In addition to early warning uses, HFSWR provides a unique ocean surface dynamics parameters remote-sensing

capability based on the Doppler spectrum characteristics of the sea echo backscattered from the ocean surface. Compared with conventional instruments such as buoys, anemometers, and line-of-sight radar, HFSWR can provide an all-time, all-weather, and cost-effective surveillance far beyond the visible horizon.

HFSWR can be classified into onshore and shipborne cases based on the platform where it is employed. Besides the advantages of onshore HFSWR, shipborne case has the agility and maneuverability, which can not only enhance the survivability in complex ocean environment but also enlarge the detection distance on open sea. Thus, ocean remote sensing with shipborne HFSWR is expected to receive increasing attentions.

The main objective of this chapter is to reveal the potential and experimental results of remote sensing of ocean surface wind field and current with shipborne HFSWR, which is organized into four sections. Section 1 describes the concept of operation for shipborne HFSWR, the general characteristics and nominal capabilities of such systems, as well as their potential roles in early warning uses and ocean remote-sensing applications. Section 2 represents the first- and second-order ocean surface cross sections derived for an omnidirectional receiving sensor in monostatic shipborne HFSWR, where the essential characteristics of the sea echo backscattered from the ocean surface are shown. Understanding the characteristics of sea echo is essential for further theoretical and experimental investigation in remote-sensing applications. Section 3 discusses the potential of remote sensing of ocean surface wind field with shipborne HFSWR. The wind field of the region covered by radar can be measured using a single receiving antenna, which is more beneficial for shipborne platform with limited deck space. Experimental results verify the detection accuracy and distance limit of the presented method. Section 4 discusses the feasibility of ocean surface current inversion in shipborne HFSWR.

2. Ocean surface cross sections for shipborne HFSWR

To investigate the potential of ocean remote sensing with shipborne HFSWR, ocean surface cross sections, which incorporates abundant ocean dynamic parameter information such as wind direction and speed, ocean surface current, and wave spectrum parameters, should be first studied. In this section, we discuss the first- and second-order ocean surface cross sections in shipborne HFSWR with a uniform linear motion [1, 2]. Moreover, we explore the effects of the radar platform motion and sea-state parameters on Doppler spectrum and present that the spreading characteristic of the first-order Doppler spectra can be utilized to resolve the wind direction ambiguity problem. Following this research, we develop the corresponding cross sections in shipborne HFSWR with both uniform linear motion and sway motion [3]. Furthermore, the effects of sway motion on Doppler spectra are discussed in detail.

2.1. First-order ocean surface cross section

2.1.1. First-order radar cross-section model

For a shipborne source, a small displacement from the origin, $\vec{\rho}_v$, is caused by the forward movement of the platform at a constant speed, as shown in **Figure 1**, ρ_1 and ρ_2 denote the
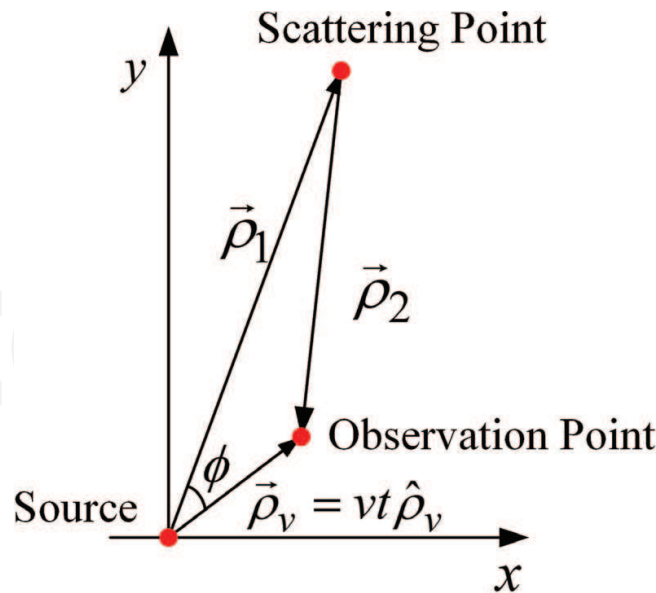
Figure 1. Geometry of the first-order scatter with platform-forward movement.

planar distances. Then, by analogy to the derivations in [4], the first-order cross section for shipborne HFSWR with a uniform linear motion is derived [1]

$$\sigma(\omega_d) = 2^6 \pi^2 k_0^4 \sum_{m=\pm1} S\left(2m\vec{k}_0\right) \delta\left(\omega_d + m\sqrt{2gk_0} - 2k_0 v \cos\phi\right) \tag{1}$$

where ω_d is the Doppler frequency, k_0 is the wavenumber of the transmitting signal, $m = \pm1$ corresponds to the receding and approaching waves, respectively, $S(\cdot)$ is the directional wave height spectrum, $\delta(\cdot)$ is the Dirac delta function, g is the gravitational acceleration, v is the speed of shipborne platform, $S(\cdot)$ can be represented as a product of a P-M spectrum [5] and a modified cardioid directional factor $G(\cdot)$ [6]. The directional factor is shown in **Figure 2**, where θ is the incident direction of echo and α^* is the wind direction. When the shipborne platform is stationary (i.e., $v = 0$), it is readily checked that the results in Eq. (1) can be reduced onshore case.

2.1.2. Experimental and simulated results

2.1.2.1. Experimental result

The fundamental data-collecting experiment was conducted on the Yellow Sea of China [7], the radar carrier frequency $f_0 = 5.283$ MHz, $\alpha^* \approx 90°$, the range resolution $\Delta\rho = 5$ km, $v = 10$ knots. The simulated result with Gaussian noise and experimental result are, respectively, displayed in **Figure 3a** and **b**.

The simulated result with Gaussian noise in **Figure 3a** indicates that the platform motion results in the spreading sea clutter spectrum, whose theoretical width is indicated by the long-dashed lines. Such a simulated spreading spectrum is confirmed by the experimental result in **Figure 3b** with the similar overall shape.
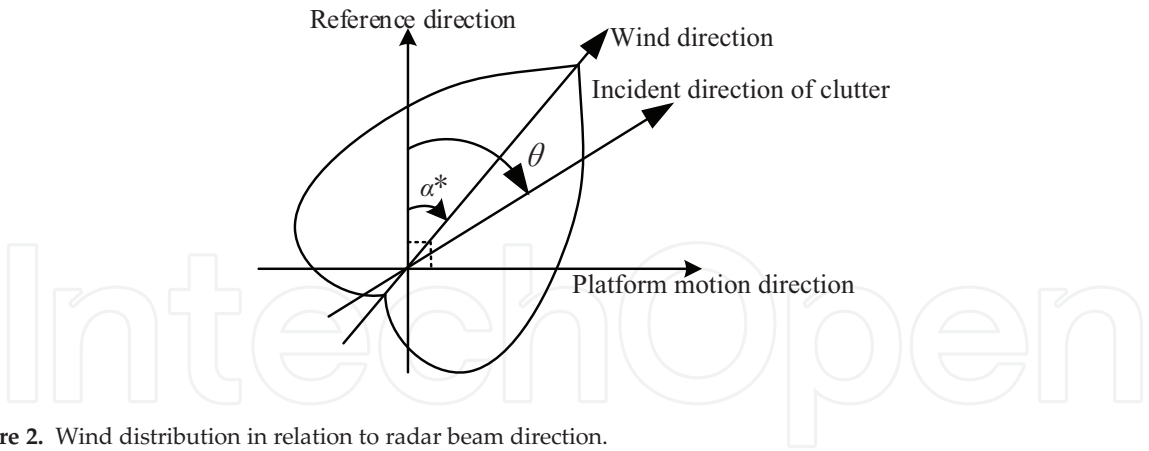
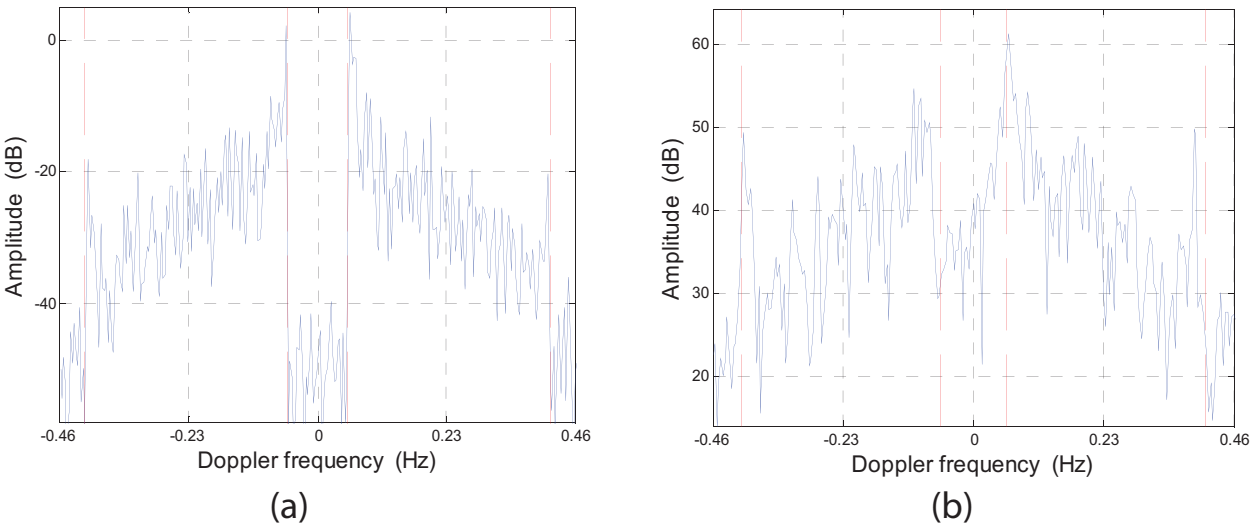**Figure 2.** Wind distribution in relation to radar beam direction.

Figure 3. First-order ocean surface cross sections: (a) simulated result and (b) experimental result.

2.1.2.2. Simulated results

Effects of the wind direction on the first-order cross section are displayed. Simulation parameters include $f_0 = 5.283\,\text{MHz}$, $\Delta\rho = 5\,\text{km}$, and $\alpha^* = 45°, 315°$. Simulation results of shipborne HFSWR for $v = 10$ knots and onshore HFSWR for $v = 0$ knots are shown in **Figure 4**.

For onshore case, the results show that the wind direction ambiguity exists, where the first-order echo has the same characteristics for different wind directions. Moreover, the first-order Bragg peaks simultaneously contain the sea clutter returns from different directions. Studies on wind direction extraction have to be conducted based on the receiving array or the compact antenna system in Coastal Ocean Dynamics Applications Radar (CODAR) system, where the problem of wind direction ambiguity is still unavoidable.

For shipborne case, however, the simulated cross sections show that the ratios of the spreading first-order Bragg lines vary with the wind directions, which demonstrates that shipborne HFSWR has the potential of wind direction extraction. Meanwhile, the wind directions of the whole sea area covered by radar may be obtained based on the spreading mechanism of the
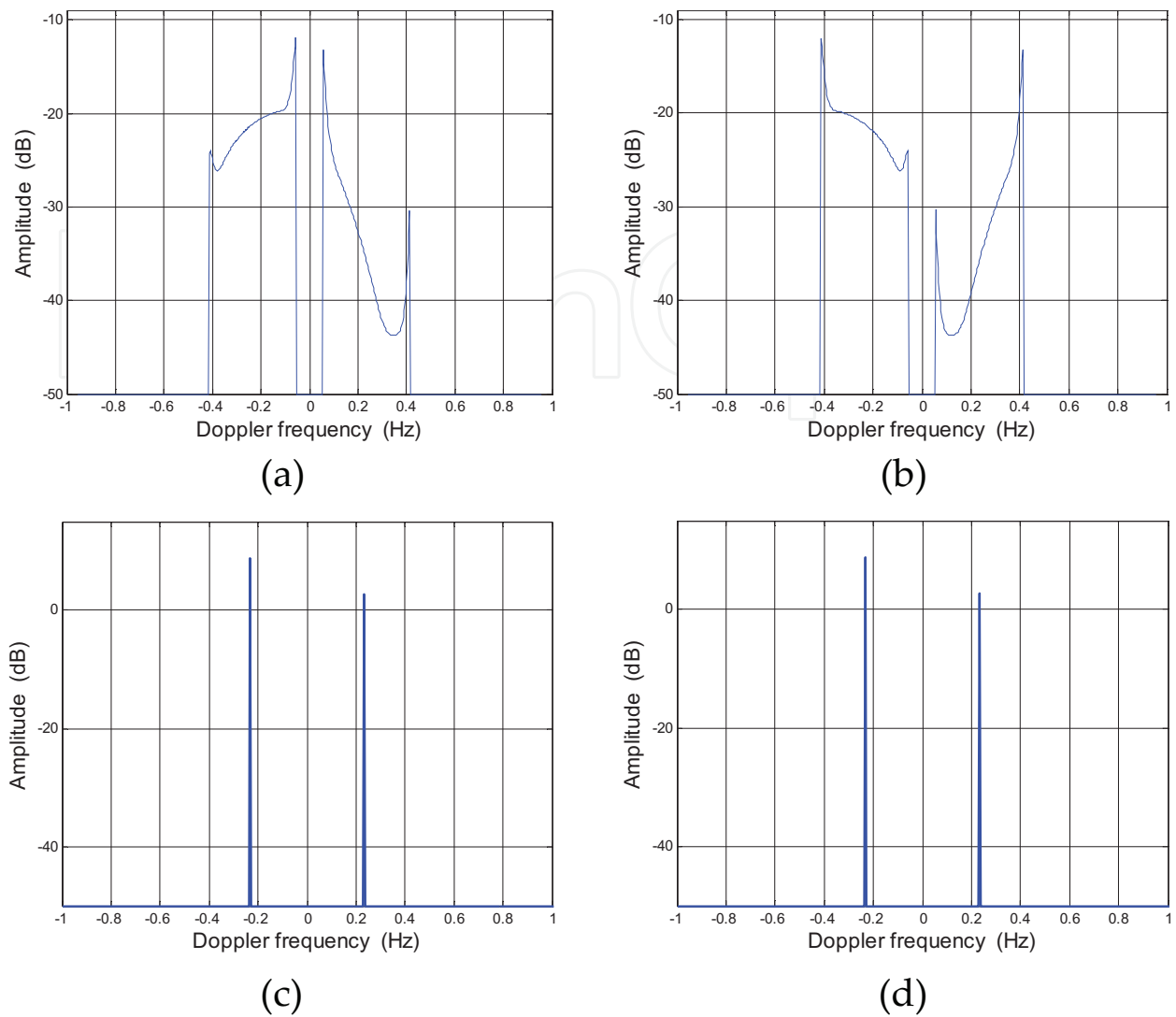
Figure 4. First-order cross section for (a) shipborne case with $\alpha^* = 45°$. (b) Shipborne case with $\alpha^* = 315°$. (c) Onshore case with $\alpha^* = 45°$. (d) Onshore case with $\alpha^* = 315°$.

first-order spectrum. Thus, compared with onshore method, it should be more easily realized in wind direction extraction by the use of a single receiving sensor instead of the receiving array.

2.2. Second-order ocean surface cross section

By analogy to the derivation in [8], the second-order cross section for shipborne HFSWR with a uniform linear motion is derived as the summation of the hydrodynamic and electromagnetic components.

2.2.1. Hydrodynamic component

The hydrodynamic component can be directly obtained by replacing the first-order ocean wave spectrum $S\left(\vec{K}, \omega\right)$ in Eq. (1) with the second-order spectrum $S_2\left(\vec{K}, \omega\right)$, which can be finally given by [2]

$$_1\sigma_2(\omega_d) = 2^6\pi^2 k_0^4 \sum_{m_1=\pm1} \sum_{m_2=\pm1} \int_{K_1}\int_{\theta_{\vec{K}_1}} |\Gamma_H|^2 S\left(m_1\vec{K}_1\right) S\left(m_2\vec{K}_2\right)$$

$$\cdot\delta\left(\omega_d - 2k_0 v\cos\phi + m_1\sqrt{gK_1} + m_2\sqrt{gK_2}\right) K_1 dK_1 d\theta_{\vec{K}_1} \qquad (2)$$

where $S_2\left(\vec{K},\omega\right) = 2\int_{\substack{\vec{K}_1+\vec{K}_2=\vec{K}\\ \omega_1+\omega_2=\omega}} S\left(\vec{K}_1,\omega_1\right) S\left(\vec{K}_2,\omega_2\right)|\Gamma_H|^2 d\vec{K}_1 d\omega_1$, and Γ_H denotes the hydrodynamic coupling coefficient. K_1 and $\theta_{\vec{K}_1}$ are the magnitude and direction of the wave vector $\vec{K}_1$, respectively. $\vec{K}_2$ is a wave vector with a magnitude of K_2. The frequencies ω_1 and ω_2 are related to $\vec{K}_1$ and $\vec{K}_2$, respectively.

2.2.2. Electromagnetic component

The second-order field equation in the time domain can be thus obtained by [2]

$$E_2(t) \approx -j\eta_0\Delta l\Delta\rho I_0 k_0^2 \frac{F^2\left(\rho_0,\omega_0\right)}{\left(2\pi\rho_0\right)^{3/2}} e^{jk_0\Delta\rho}$$

$$\cdot\sum_{\vec{K}_1}\sum_{\vec{K}_2} \sqrt{K}\Gamma_{EM} P_{\vec{K}_1} P_{\vec{K}_2} e^{-j\pi/4} e^{jK\rho_0} e^{jvtK\cos\phi} \text{Sinc}\left[\frac{\Delta\rho}{2}(K-2k_0)\right] \qquad (3)$$

where η_0 is the intrinsic impedance, I_0 is the peak current for a dipole with length Δl, $k_0 = \omega_0/c$, ω_0 is the radian frequency, $\rho_0 = c(t-\tau_0/2)/2$, $\Delta\rho = c\tau_0/2$, c is the speed of light, and τ_0 is the length of the pulse. Sinc$(\cdot)$ denotes the sinc function. $P_{\vec{K}_1}$ and $P_{\vec{K}_2}$ are random variables corresponding to the wave vectors $\vec{K}_1$ and $\vec{K}_2$, respectively. $\vec{K} = \vec{K}_1 + \vec{K}_2$, $F(\cdot)$ is the Sommerfeld attenuation function, and Γ_{EM} is the electromagnetic coupling coefficient.

The autocorrelation function with respect to the time shift τ is given by

$$R(\tau) = \left\langle E_2(t+\tau)E_2^*(t)\right\rangle \cdot A_r/2\eta_0 \qquad (4)$$

where $(\cdot)^*$ and $\langle\cdot\rangle$ are the complex conjugate and statistical average, $A_r = \lambda_0^2 G_r/4\pi$, G_r is the antenna gain, and λ_0 is the wavelength.

Then, Eq. (4) can be finally simplified as

$$R(\tau) = \frac{\lambda_0^2}{4\pi}\frac{G_r}{2\eta_0}\left\{\frac{\eta_0^2\Delta l^2\Delta\rho^2 I_0^2 k_0^4 F^4\left(\rho_0,\omega_0\right)}{\left(2\pi\rho_0\right)^3} \sum_{m_1=\pm1}\sum_{m_2=\pm1} \int_K\int_{\theta_{\vec{K}}}\int_{K_1}\int_{\theta_{\vec{K}_1}} K^2|\Gamma_{EM}|^2\right.$$

$$\cdot\frac{1}{2}S\left(m_1\vec{K}_1\right) S\left(m_2\vec{K}_2\right) e^{jKv\tau\cos\phi} e^{-jm_1\sqrt{gK_1}\tau} e^{-jm_2\sqrt{gK_1}\tau}$$

$$\left.\cdot\text{Sinc}^2\left[\frac{\Delta\rho}{2}(K-2k_0)\right]\right\} K_1 dK_1 d\theta_{\vec{K}_1} d\theta_{\vec{K}} \qquad (5)$$

A Fourier transform of Eq. (5) yields the power density spectrum. Then, the second-order ocean surface cross section can be calculated by normalizing the power density spectrum per unit area, which is simplified by [2]

$$
{}_2\sigma_2(\omega_d) = 2^6\pi^2k_0^4 \sum_{m_1=\pm1}\sum_{m_2=\pm1}\int_{K_1}\int_{\theta_{\vec{K_1}}}|\Gamma_{EM}|^2S(m_1\vec{K_1})S(m_2\vec{K_2})
$$
$$
\cdot\delta(\omega_d - 2k_0v\cos\phi + m_1\sqrt{gK_1} + m_2\sqrt{gK_2})K_1dK_1d\theta_{\vec{K_1}} \tag{6}
$$

2.2.3. Total second-order ocean surface cross section

Apart from the coupling coefficients, the hydrodynamic and electromagnetic cross sections in Eqs. (2) and (6) are identical. Thus, the total second-order ocean surface cross section in shipborne HFSWR can be written as [2]

$$
\sigma_2(\omega_d) = 2^6\pi^2k_0^4 \sum_{m_1=\pm1}\sum_{m_2=\pm1}\int_{K_1}\int_{\theta_{\vec{K_1}}}|\Gamma|^2S(m_1\vec{K_1})S(m_2\vec{K_2})
$$
$$
\cdot\delta(\omega_d - 2k_0v\cos\phi + m_1\sqrt{gK_1} + m_2\sqrt{gK_2})K_1dK_1d\theta_{\vec{K_1}} \tag{7}
$$

where the total coupling coefficient $\Gamma = \Gamma_H + \Gamma_{EM}$.

2.2.4. Simulation results

2.2.4.1. Simulated cross sections for different platform speeds

Simulation parameters: $f_0 = 5.283\,\text{MHz}$, $\alpha^* = 90°$, and wind speed $U = 15\,\text{knots}$. From **Figure 5a**, the Bragg peaks are located at $f_{B,M} = \pm0.2344\,\text{Hz}$, and the $\sqrt{2}f_{B,M}$ peaks (the harmonic peaks) and $2^{3/4}f_{B,M}$ peaks (the electromagnetic "corner reflector" peaks) are also visible. From Eqs. (1) and (7), sea echoes at different incident directions correspond to different Doppler frequencies because an angle ϕ exists between echo incident direction and the direction of the platform-forward movement. That is, the radar Doppler spectra are spread, as
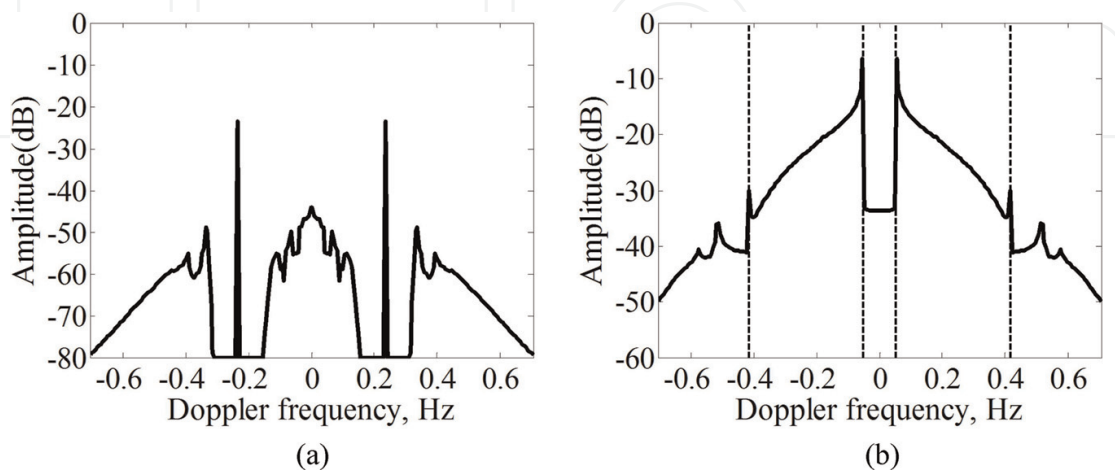

Figure 5. Simulated cross sections for (a) onshore case and (b) shipborne case with $v = 10$ knots.
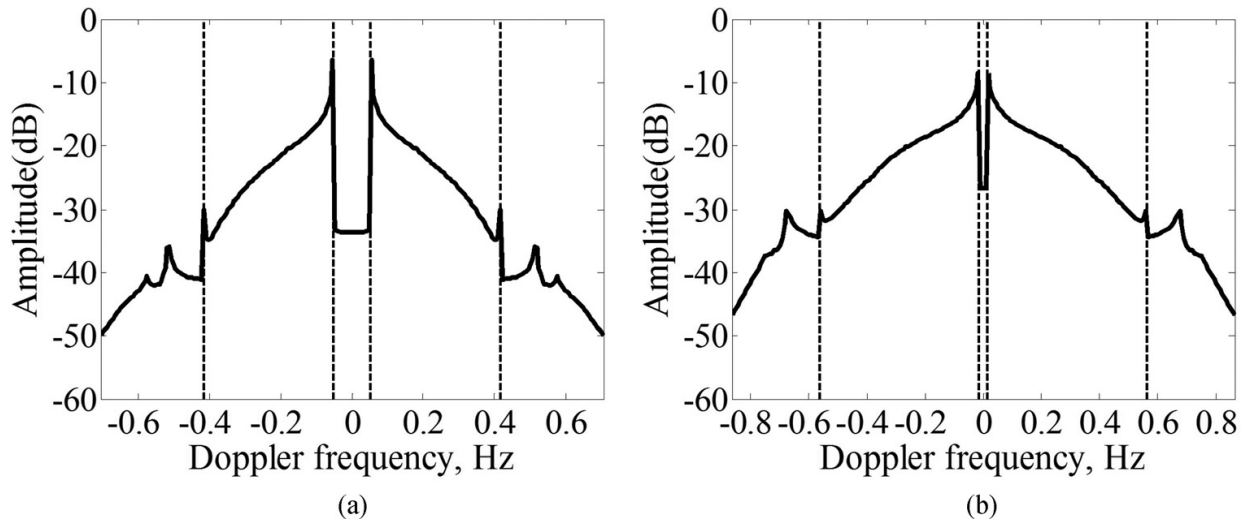
Figure 6. Simulated cross sections for (a) $f_0 = 5.283$ MHz and (b) $f_0 = 8$ MHz.

shown in **Figure 5b**. The dashed lines denote the theoretical spreading domains of the first-order sea clutter Doppler spectrum.

2.2.4.2. Simulated cross sections for different radar frequencies

Simulation parameters: $U = 15$ knots, $v = 10$ knots, and $\alpha^* = 90°$. From **Figure 6**, the spreading domain increases and the energies of the second-order spectra increase with the increasing radar frequency. This shows that a high radar frequency may be negative for moving target detection and remote sensing.

2.2.4.3. Simulated cross sections for different wind speeds

Simulations parameters: $\alpha^* = 90°$, $v = 10$ knots, and $f_0 = 5.283$ MHz. Simulation results show that the energies of the first- and second-order spectra increase as the wind speed increases, as
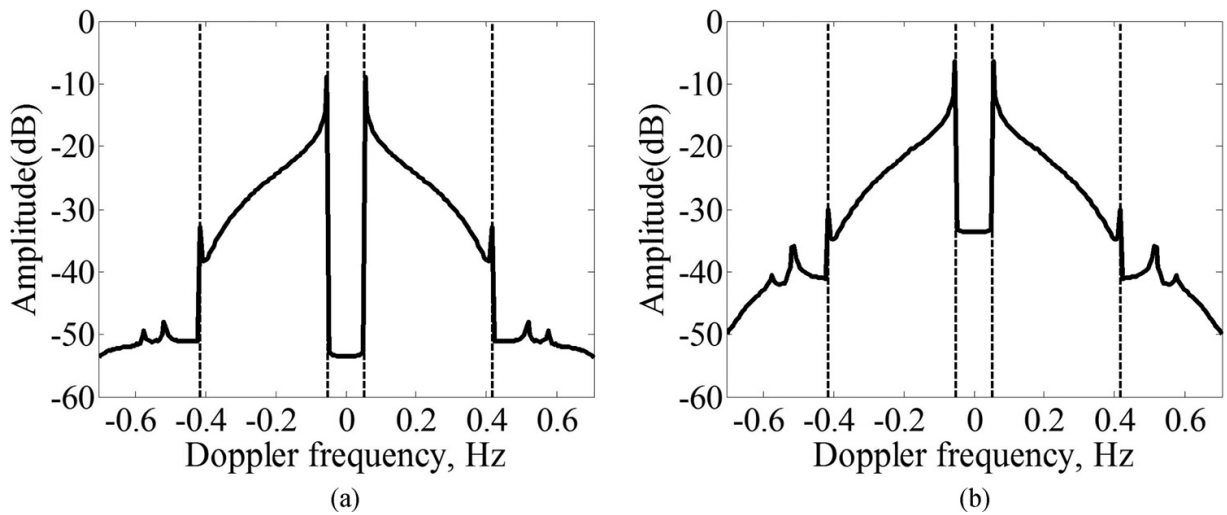

Figure 7. Simulated cross sections for (a) $U = 12$ knots and (b) $U = 15$ knots.

shown in **Figure 7**. The first- and second-order spectra may be overlapped when the wind speed is high, which may be unfavorable for remote sensing of ocean surface wind direction and speed. This is because the wind direction is extracted from the ratio of the positive and negative Bragg energies, and the wind speed relates to the energies of the second-order backscatter echo.

2.2.4.4. Simulated cross sections for different wind directions

Simulation parameters: $U = 15\,$knots, $v = 10\,$knots, and $f_0 = 5.283\,$MHz. From **Figure 8**, it is apparent that the spreading first-order Bragg lines vary with wind direction. However, the Bragg line energies may be contaminated by the second-order contributions. Thus, the high sea state may influence wind direction extraction from the spreading Bragg lines in shipborne HFSWR.

2.3. Ocean surface cross sections for shipborne HFSWR with sway motion

In practice, the shipborne platform exists six-degree-of-freedom (DOF) motion due to the interaction between the platform and the complicated ocean environment. In this subsection, following the research in the previous subsection, we derive corresponding cross sections which incorporate both the uniform linear motion and the sway motion [3].

2.3.1. First-order cross section

For a shipborne source in **Figure 9**, the small displacement $\delta\vec{\rho}$ from the origin is induced by the uniform linear motion $\vec{\rho}_v = vt\hat{\rho}_v$ and the sway motion $\delta\vec{\rho}_0 = a\sin\left(\omega_p t\right)\hat{\rho}_p$. Following the above-mentioned research, the first-order cross section can be written as [3]
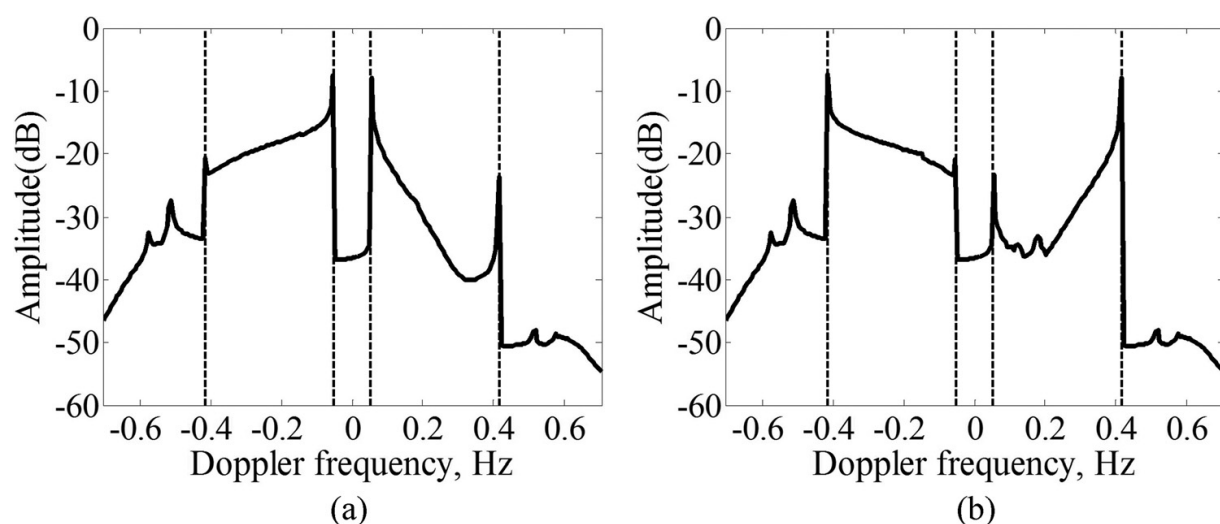

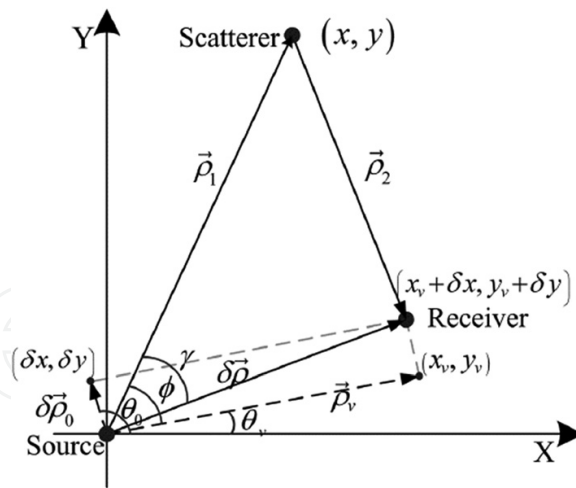**Figure 8.** Simulated cross sections for (a) $\alpha^* = 45°$ and (b) $\alpha^* = 315°$.

Figure 9. First-order scatter geometry in shipborne HFSWR with sway motion.

$$\sigma_1(\omega_d) = 2^6 \pi^2 k_0^4 \sum_{m=\pm 1} S\left(2m\vec{k}_0\right) \left\{ J_0^2[2ak_0 \cos(\theta_k - \theta_0)] \right.$$

$$\cdot \delta\left(\omega_d + m\sqrt{2gk_0} - 2k_0 v \cos\phi\right) + \sum_{n=1}^{\infty} J_n^2[2ak_0 \cos(\theta_K - \theta_0)]$$

$$\left. \cdot \left[\delta\left(\omega_d + m\sqrt{2gk_0} - 2k_0 v \cos\phi - n\omega_p\right) + \delta\left(\omega_d + m\sqrt{2gk_0} - 2k_0 v \cos\phi + n\omega_p\right)\right] \right\} \quad (8)$$

where ω_p and a are the sway frequency and amplitude related to sea state, respectively. $\hat{\rho}_p$ is the unit vector of $\delta\vec{\rho}_0$, $J_n(\cdot)$ represents the nth order Bessel function, and θ_K is the direction of the wave vector $\vec{K}$.

2.3.2. Second-order cross section

Similar to the derivation in Section 2.2, the second-order cross section for this new shipborne platform motion model can be derived as [3]

$$\sigma_2(\omega_d) = 2^6 \pi^2 k_0^4 \sum_{m_1=\pm 1} \sum_{m_2=\pm 1} \int_{K_1} \int_{\theta_{\vec{K}_1}} |\Gamma|^2 S\left(m_1\vec{K}_1\right) S\left(m_2\vec{K}_2\right)$$

$$\cdot \left\{ J_0^2[2ak_0 \cos(\theta_k - \theta_0)]\delta\left(\omega_d + m_1\sqrt{gK_1} + m_2\sqrt{gK_2} - 2k_0 v \cos\phi\right) \right.$$

$$+ \sum_{n=1}^{\infty} J_n^2[2ak_0 \cos(\theta_K - \theta_0)]\delta\left(\omega_d + m_1\sqrt{gK_1} + m_2\sqrt{gK_2} - 2k_0 v \cos\phi - n\omega_p\right)$$

$$\left. + \delta\left(\omega_d + m_1\sqrt{gK_1} + m_2\sqrt{gK_2} - 2k_0 v \cos\phi + n\omega_p\right) \right\} K_1 dK_1 d\theta_{\vec{K}_1} \quad (9)$$

2.3.3. Simulation results

For convenience, the sea echo Doppler spectral cross section is decomposed as the sum of the first- and second-order scattering terms

$$\sigma(\omega_d) = \sigma_1(\omega_d) + \sigma_2(\omega_d) \qquad (10)$$

It can be inferred from Eq. (10) that the derived cross sections could be reduced to the existing results. Specifically, in the case of no uniform linear motion (i.e., $v = 0$), it is readily checked that the derived expressions are consistent with Walsh's results for an antenna on a floating platform [4, 8]. For the platform without sway motion (i.e., $a = 0$), Eq. (10) agrees well with Xie's results [1, 2]. For $a = 0$ and $v = 0$, it is possible to reduce the derived results to the well-known cross sections derived by Barrick [5, 9] or Walsh [10] for onshore monostatic HF radar. This means that the derived cross section can be reasonably regarded as Xie's results in shipborne HFSWR are modulated by sway motion, or Walsh's results in HF radar on a floating platform are spread due to a uniform linear motion.

2.3.3.1. Cross sections for different platform speeds

Simulation parameters: $f_0 = 5.283\,\text{MHz}$, $\alpha^* = 90°$, and $U = 15\,\text{knots}$. In **Figure 10**, A and A' indicate the Doppler frequencies of sea echo with $\phi = 0$, whereas B and B' represent the Doppler frequencies of sea echo with $\phi = \pi$. For a given radar-operating frequency in Eq. (10), it is evident that the broadening region of the first-order sea echo is proportional to v. Because such Doppler spreading can potentially mask the target echo of interest, a significant challenge in shipborne HFSWR is the detection of moving targets whose Doppler frequencies appear in the spreading region. When the platform moves at a high speed, the first-order sea echo spectrum will overlap. To avoid the effect of Doppler overlap on wind direction extraction with shipborne HFSWR, the platform speed should be limited by a theoretical maximum value $v_{\max} = \sqrt{g\lambda_0/(4\pi)}$. Additionally, it can be inferred that additional spectra induced by sway motion will repeatedly emerge and be located with uniform spacing of sway frequency, as shown in **Figure 10**.

2.3.3.2. Cross sections for different wind directions

Simulation parameters: $f_0 = 5.283\,\text{MHz}$, $U = 15\,\text{knots}$, and $v = 10\,\text{knots}$. From **Figure 11**, there exists obvious envelop distortion in the Doppler spectrum, which is indicated by the circles. Under this condition, the positive and negative Bragg line energies are contaminated by the second-order contributions [2], and the "corner reflector" peaks in the positive Doppler
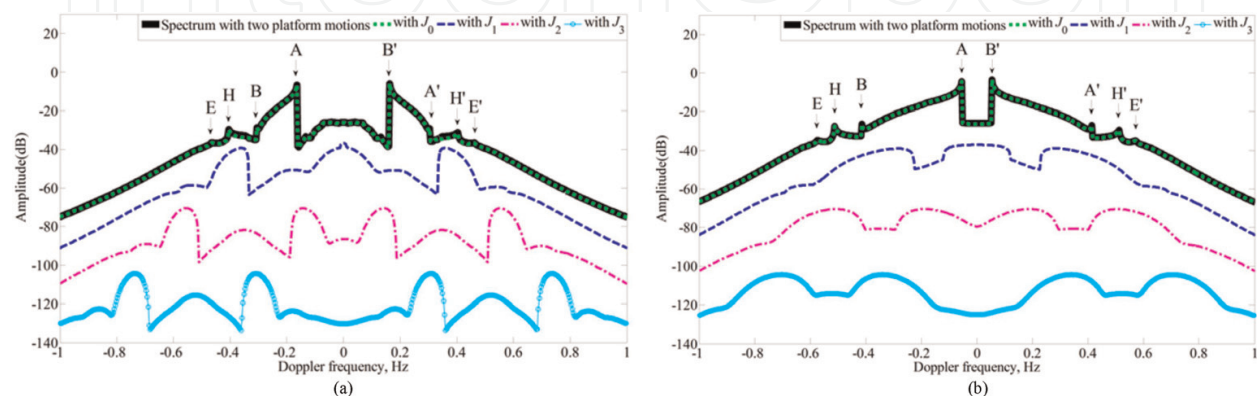

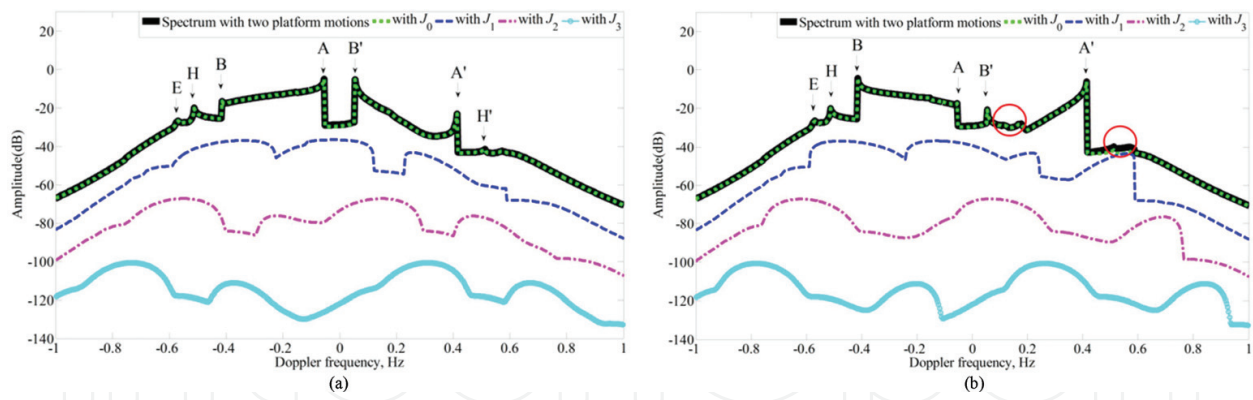**Figure 10.** Simulated cross sections for (a) $v = 4$ knots and (b) $v = 10$ knots.

Figure 11. Simulated cross sections for different wind directions. (a) $\alpha^* = 45°$ and (b) $\alpha^* = 315°$.

spectrum are also masked by these sway-induced contributions. In remote-sensing applications, the sea echoes scattered from the ocean surface could be interpreted to extract the wave height spectrum, as well as to estimate the surface current and wind field. Therefore, the envelop distortions in the Doppler spectra may degrade the performance of ocean remote sensing. Specifically, this would be detrimental to the wind direction extraction from the ratio of the positive and negative Bragg line energies in shipborne HFSWR.

3. Remote sensing of ocean surface wind field with shipborne HFSWR

In this section, the potential of remote sensing of ocean surface wind direction and speed with shipborne HFSWR are presented [11, 12], respectively. Based on the spreading mechanism of the first-order Bragg lines, the unambiguous wind direction is extracted by the use of a single receiving sensor. Due to this single-side system consisting of a transmitter and a receiving sensor, it can be realized more easily and with less system cost, and it is more suitable for a shipborne platform with limited deck space.

3.1. Space: time distributions of first-order sea echo

From Eq. (1), it can be inferred that the locations of positive and negative Bragg lines are determined by the angle ϕ, which is consistent with the space-time distribution of the first-order sea clutter [7]

$$f_d = f_{dp} \cos \phi \pm f_B \tag{11}$$

where $f_d = \omega_d / 2\pi$, $f_{dp} = 2v/\lambda$, $f_B = \sqrt{g/\pi\lambda}$ is the first-order Bragg frequency in monostatic onshore HFSWR. Different Doppler frequencies in Bragg region correspond to the sea echoes from different incident directions and vice versa; therefore, the first-order Doppler spectrum is

spread due to the forward movement of the platform. Then, the spreading domains of the first-order Doppler spectrum should be

$$\left[-f_B - 2v/\lambda, -f_B + 2v/\lambda\right], \quad \left[f_B - 2v/\lambda, f_B + 2v/\lambda\right] \tag{12}$$

Taking the differential of f_d in Eq. (11), the Doppler frequency resolution Δf_d can be expressed as a function of the azimuth resolution $\Delta\phi$, which can be expressed as

$$\Delta f_d = f_{dp} \sin\phi \cdot \Delta\phi \tag{13}$$

Analogously to Doppler beam sharpening (DBS), the azimuth resolution can be obtained by

$$\Delta\phi = \Delta f_d / \left(f_{dp} \sin\phi\right) \quad \text{for } \phi \neq 0 \tag{14}$$

Generally, HFSWR can provide a very high-frequency resolution with long coherent integration time (CIT). Therefore, the shipborne HFSWR may provide a higher transverse resolution than onshore HFSWR with a huge antenna array aperture.

3.2. Wind direction extraction in shipborne HFSWR

3.2.1. Mathematical model

For onshore HFSWR, wind directions are sensitive to the ratio of energies of positive and negative Bragg peaks, which can be used to measure the wind direction [13]. To extract the wind direction with shipborne HFSWR, analogously to onshore HFSWR case, the ratio R of the positive and negative Bragg lines energies, B^+ and B^-, is defined by

$$R = 10 \cdot \log_{10}(B^+/B^-) \tag{15}$$

where $\frac{B^+}{B^-} = \frac{\sigma(\omega_d)}{\sigma(-\omega_d)} = \frac{G(\theta + \pi - \alpha^*)}{G(\theta - \alpha^*)}$. The application prerequisite of Eq. (15) is that the two spreading domains of the first-order Doppler spectrum in Eq. (12) are not overlapped, which means the maximum permitted speed of shipborne platform $v_{\max} = \sqrt{g\lambda/(4\pi)}$.

Together with the modified cardioid directional factor in Eq. (1), the abovementioned ratio can be finally simplified as

$$R = 10\log_{10}\left(\frac{\xi + (1 - \xi)\sin^4\left(\frac{\theta - \alpha^*}{2}\right)}{\xi + (1 - \xi)\cos^4\left(\frac{\theta - \alpha^*}{2}\right)}\right) \tag{16}$$

where $\xi = 0.004$ is the strength ratio of upwind returns to downwind returns. For the convenience of description of Eq. (16), we can define y as

$$y = \sin^2\left(\frac{\theta - \alpha^*}{2}\right) \tag{17}$$

Therefore, once y is calculated from Eq. (16), possible wind directions can be deduced by

$$\alpha_p^* = \theta \pm 2\arcsin\left(\sqrt{y}\right) \tag{18}$$

where $\pm$ sign indicates the wind direction ambiguity.

3.2.2. Method for resolving wind direction ambiguity

For a fully developed sea area, wind directions are generally considered to be spatially uniform or slow-varying over adjacent ocean patch. That means the differences of wind directions in adjacent ocean patches should be zero or near zero. **Figure 12a** describes four adjacent ocean patches with corresponding incident directions. For ocean patch A with the incident direction ϕ_A, the energies of positive and negative Bragg lines can be derived, as shown in **Figure 12b**. Then, two possible wind directions α_{A1}^* and α_{A2}^* can be calculated by Eq. (18). Similarly, the possible wind directions α_{B1}^* and α_{B2}^* for ocean patch B can also be derived. We define

$$\Delta\alpha_{ij} = \left|\alpha_{Bi}^* - \alpha_{Aj}^*\right| \quad (i,j = 1,2) \tag{19}$$

The value of α_{Bi}^* that minimizes $\Delta\alpha_{ij}$ is considered as the real wind direction of ocean patch B. Therefore, the wind directions of the whole ocean area covered by radar can be measured by sequentially applying this method.

3.2.3. Simulation and discussion

3.2.3.1. Simulation for wind direction extraction

Simulation parameters:$f_0 = 5.283\,\text{MHz}$, $v = 10\,\text{knots}$. Consider that the input wind direction α^* slowly increasing from 135˚ to 180˚ is given for simulation. Due to the directional ambiguity, it is difficult to determine the unique wind direction from the two possible solutions with a single incident direction ϕ as shown in **Figure 13a**. However, the problem of wind direction
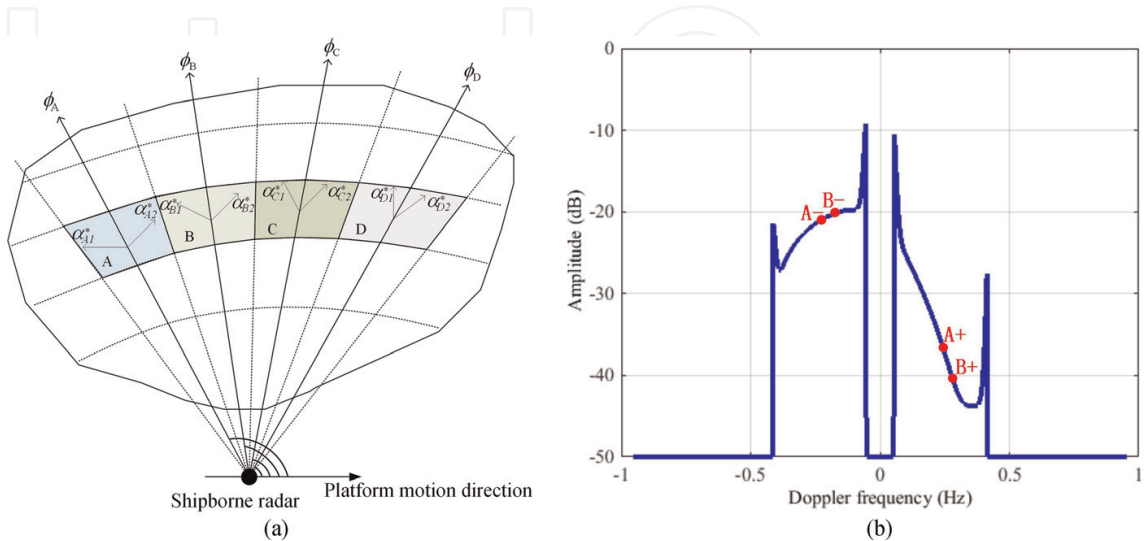

Figure 12. (a) Possible wind directions of four spatially adjacent ocean patches A, B, C, and D. (b) Doppler spectrum.

ambiguity can be effectively removed by comparing the possible results of adjacent sea cells, as shown in **Figure 13b**, where the circles denote the slow-varying wind directions for simulation. Simulation results visually illustrate the process of removing the directional ambiguity, and the good agreement between the derived wind direction and the simulation parameter shows the potential of unambiguity wind direction extraction with shipborne HFSWR.

3.2.3.2. Discussions of basic applications in shipborne HFSWR

In experiment, the effects of the coverage region shift due to platform motion, the real sailing conditions (fluctuations of platform speed and course) during CIT, and the external Gaussian noise on the wind direction extraction should be studied.

3.2.3.2.1. Effect of covered region shift due to platform motion

In order to investigate the effect of covered region shift, the ratio R_{shift} is defined as

$$R_{shift} = \frac{\Delta r}{\Delta R} \qquad (20)$$

where $\Delta r = vT$ is the covered region shift during CIT T, $\Delta R = \Delta\phi \cdot \rho$ is the transverse resolution, $\Delta\phi$ is the azimuth resolution in Eq. (14), and ρ is the radar detection range.

Then, Eq. (20) can be rewritten as

$$R_{shift} = \frac{2v^2T^2 \sin\phi}{\lambda\rho} \leq \frac{2v^2T^2}{\lambda\rho} \qquad (21)$$

Reviewing the typical radar parameters in [7]: $f_0 = 5.283\,\mathrm{MHz}$, $v = 10\,\mathrm{knots}$, $\rho = 100\,\mathrm{km}$, and $T = 150\,\mathrm{s}$, $R_{shift} < 0.21$ can be obtained. That means Δr is nearly one-fifth of ΔR during T. In addition, wind directions are considered to be uniform or slow-varying within adjacent ocean patches. As mentioned earlier, we consider that the covered region shift during T would not significantly influence the presented method.
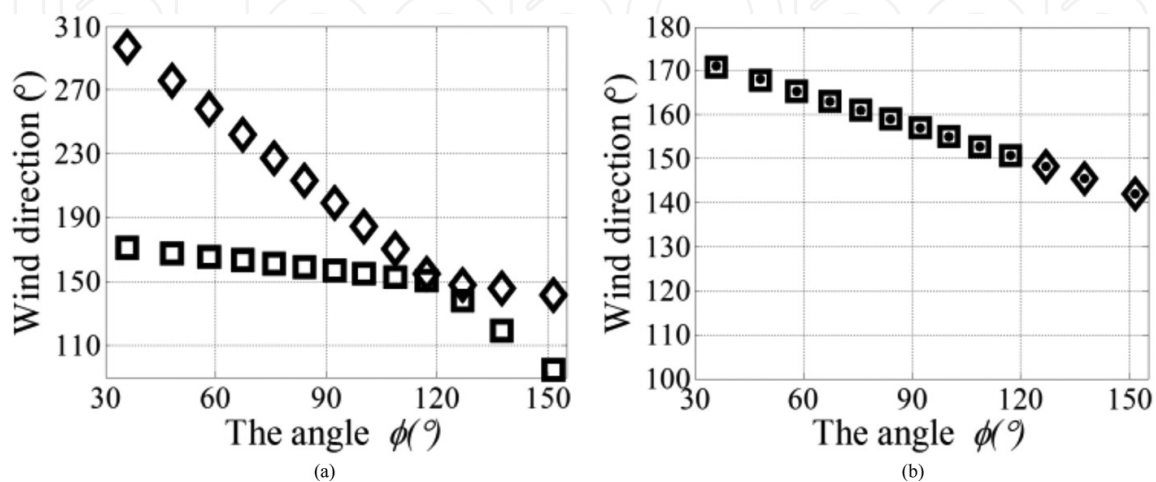

Figure 13. (a) Possible wind directions. (b) Determination of unique wind direction.

3.2.3.2.2. Effect of real sailing conditions

In order to explore the effect of real sailing conditions, the sailing data [7] are exploited to derive the synthetic Doppler spectra. For comparison, then, the ideal Doppler spectra also are derived. The simulation parameters are $f_0 = 5.283\,\mathrm{MHz}$, $v = 10\,\mathrm{knots}$, $\alpha^* = 90°$, and $U = 25\,\mathrm{knots}$.

A comparison of the ideal and synthetic spectra shows that the spreading regions of the latter are slightly more obvious, as shown in **Figure 14**. Although slight fluctuation exists in the speed and course, no apparent differences are found between the ideal and synthetic spectra except for the margin. In experiment, accordingly, the middle regions of the spreading spectra (e.g., $\phi \in [30°, 150°]$) should be exploited to measure the wind direction.

3.2.3.2.3. Effect of external Gaussian noise

To examine the performance of the proposed method in externally noise-limited environment, time series of the backscattered electric field is provided as follows:

$$(E_n)_1(\phi, t) = M \cdot \sum_{\vec{K}, \omega} P_{\vec{K}, \omega} \sqrt{K} e^{j\omega t} e^{j(\rho + vt\cos\phi)K} \Delta\rho \operatorname{sinc}\left[(K - 2k_0)\Delta\rho/2\right] \tag{22}$$

where M is a constant, $P_{\vec{K}, \omega}$ is Fourier coefficients of ocean surface components, K and ω are the wavenumber and radian angular frequency, respectively, $\Delta\rho$ is the range resolution, and $\operatorname{Sinc}(\cdot)$ is the sinc function.

The spreading spectra with the Gaussian noise can be derived by a periodogram method [14, 15]. The simulated spectra from 150 s time series are shown in **Figure 15**, where $f_0 = 5.283\,\mathrm{MHz}$, $\rho = 100\,\mathrm{km}$, $v = 5.07\,\mathrm{m/s}$, $\Delta\rho = 5\,\mathrm{km}$, and α^* slowly increasing from $0°$ in the stern to $45°$ at the prow of shipborne platform. It is obvious that the noise floors decrease with the increasing signal-to-noise ratio (SNR). That means a high SNR can improve the performance of the wind direction estimation.
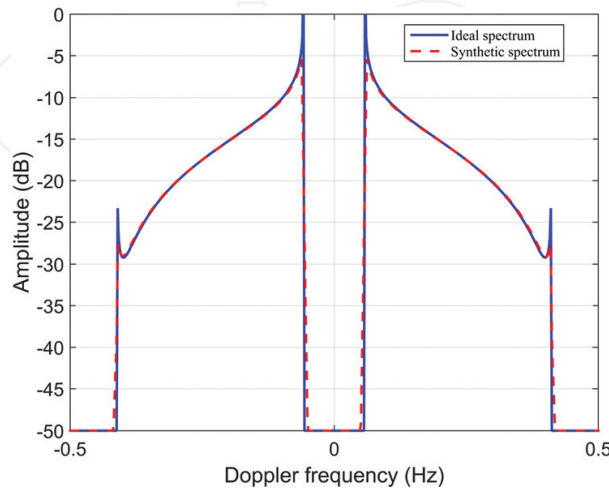

Figure 14. Ideal and the synthetic spreading Doppler spectra.

3.2.3.2.4. Effect of comprehensive factors

Together with the real sailing speed and heading data, the influence of external noise is shown in **Figure 16**. The performance is estimated via 100 independent Monte Carlo simulations for each SNR, where the simulation parameters are the same as those in **Figure 15**. It is apparent that the error of the wind direction estimation gradually decreases with the increasing SNR. There is no obvious deviation between the two error curves. Therefore, external Gaussian noise is the major factor affecting the performance of the wind direction estimation.

3.2.4. Experimental results

Shipborne HFSWR data were collected for moving target detection on 26 September 2016, in Taiwan Strait, China, by the Harbin Institute of Technology with a carrier frequency of
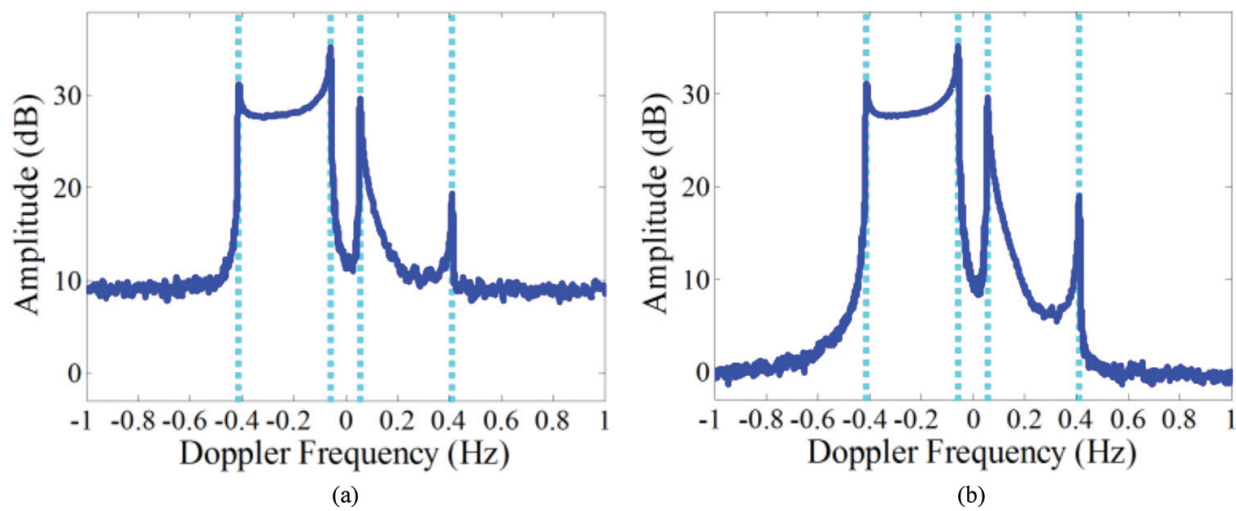

Figure 15. Simulated spreading spectra with Gaussian noise: (a) SNR = 10 dB and (b) SNR = 20 dB.
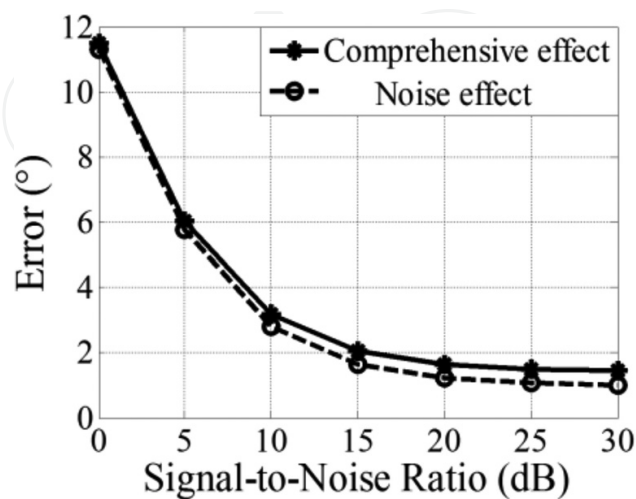

Figure 16. Wind direction error caused by external Gaussian noise and comprehensive factors.

6.45 MHz. Due to the directional ambiguity problem, partial data collected by shipborne HFSWR sailing along the coast with a suitable speed can be exploited to validate the proposed method.

In this experiment, the data collected by a single antenna during CIT from 08:47:37 to 08:49:46 were used for wind direction extraction. The average speed of the platform is 4.67 m/s. The CIT is 129 s and the number of pulse during CIT is 512. The signal bandwidth is 50 kHz. The detection limit and azimuth are 120 km and 53.4°–151.1° north, respectively. It should be noted that an integral shift method is used to alleviate the effect of ocean surface current.

The radar-measured wind direction results are shown in **Figure 17**. Forecast data supported by the FUJIAN MARINE FORECASTS (FJMF) are exploited to preliminarily validate the performance of the presented method because of the lacking of in situ data. A comparison of **Figures 17** and **18** shows that the radar-measured results agree well with the local wind direction forecasts over the same period. Given the data-observed time, **Figure 18a** is considered as the reference of the real wind field. That is, "real" wind directions are slow-varying from 27.5° to 10.6° northeast, and "real" wind speeds are slow-varying from 13.8 to 8 m/s in the detection region form north to south. A histogram of radar-measured wind direction results is shown in **Figure 19**. Only samples whose sampling number is greater than 10 are exploited to verify the performance of the wind direction measurement; 55.42% of the radar-measured results are located in the range of the "real" wind direction. The percentage can achieve 90.07% if the "real" wind direction range is extended to 0.6°–37.5° northeast. Meanwhile, the average value and the root-mean-square error (RMSE) of the radar-measured results are 14.56° northeast and 9.85°, respectively.
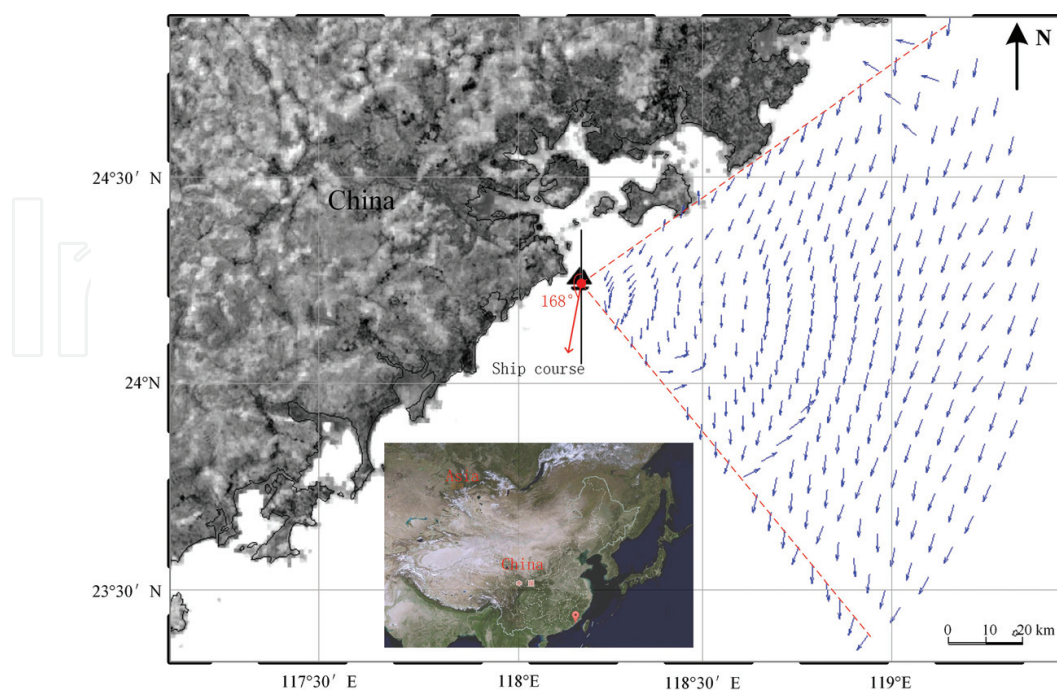

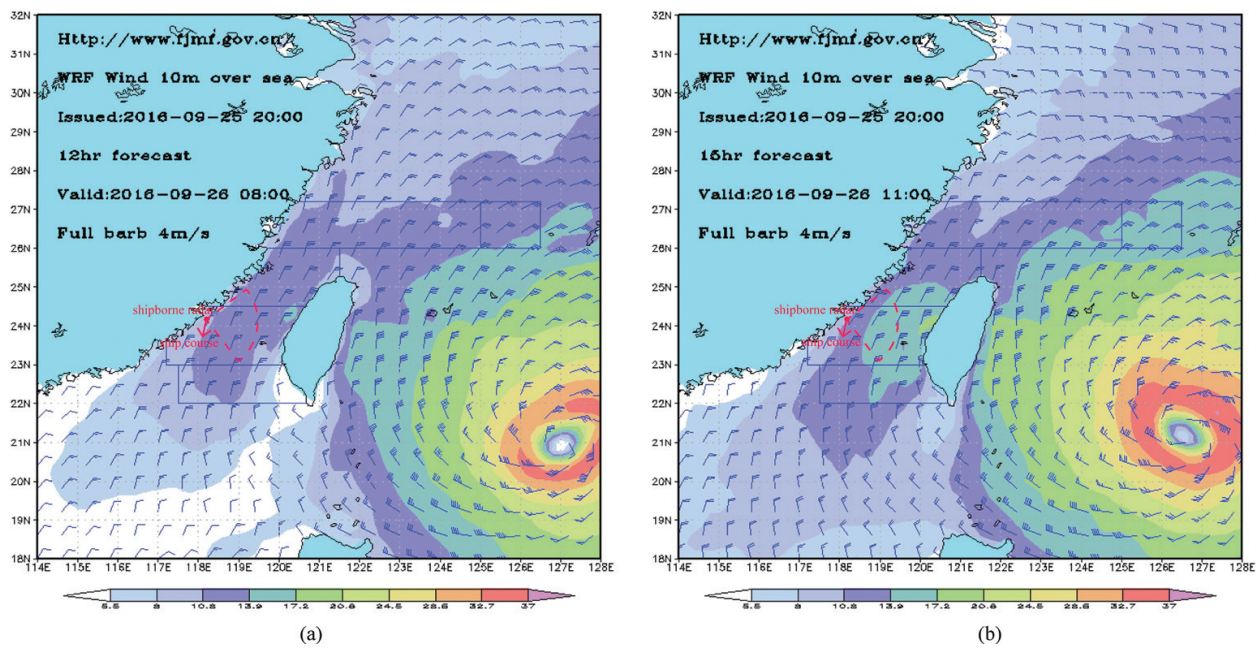**Figure 17.** Wind direction map derived by shipborne HFSWR. Dot: Shipborne radar. Arrow: Ship course.

Figure 18. Wind field map at (a) 8:00 and (b) 11:00 on September 26, 2016. Dot: Shipborne radar.
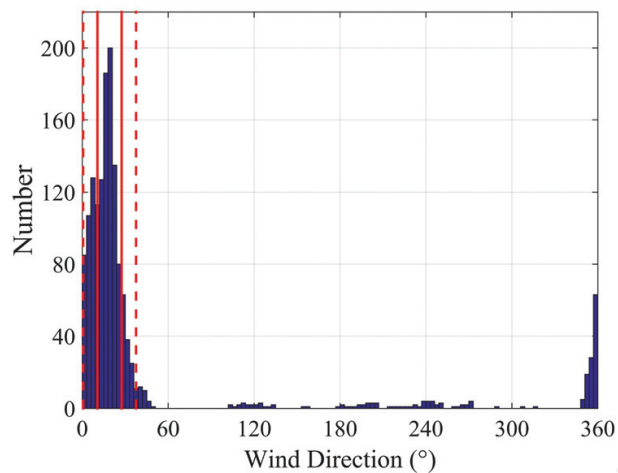

Figure 19. Histogram of derived wind directions for the degree interval of 3° each.

3.3. Wind field extraction in shipborne HFSWR

In Section 3.2, we proposed a method for extracting the unambiguous wind direction with an empirical spreading parameter value of 2. In view of [16, 17], the spreading parameter depends on the wind speed, which may be variable in the experiment. The optimum value for the spreading parameter should be estimated from the shipborne HFSWR experiment data itself. In this section, a method for simultaneously deriving the unambiguous wind direction and the unique spreading parameter will be presented. Then, a relationship between the wind speed and the spreading parameter will be developed by the drag coefficient. Therefore, the wind field can be measured by sequentially using the presented method.

3.3.1. Method for deriving unambiguous wind direction

Assuming that the spreading parameter s is a variable argument, analogously to Section 3.2.2, Eq. (15) can be rewritten as

$$R = 10 \log_{10} \left(\frac{\xi + (1 - \xi)y^s}{\xi + (1 - \xi)(1 - y)^s} \right) \tag{23}$$

where

$$y = \sin^2 \left(\frac{\theta - \alpha^*}{2} \right) \tag{24}$$

Therefore, the possible wind directions can be deduced by

$$\alpha_p^* = \theta \pm 2 \arcsin \left(\sqrt{y} \right) \tag{25}$$

where α_p^* varies with s, the $\pm$ sign indicates the ambiguity of wind direction.

For each incident direction of sea echoes, analogously to Section 3.2.3, the derived wind directions for different spreading parameters can be determined by Eq. (25), as shown in **Figure 20a**. Obviously, the intersection of these two curves should be the unique solution for the wind direction and the spreading parameter. **Figure 20b** shows a two-solution case, and then the sea echo at the third incident direction from the adjacent cell will be necessary to determine the unique solution.

3.3.2. Method for calculating wind speed

A relationship between s and the wind speed U is developed by a momentum transfer factor μ, which can be written as [18]
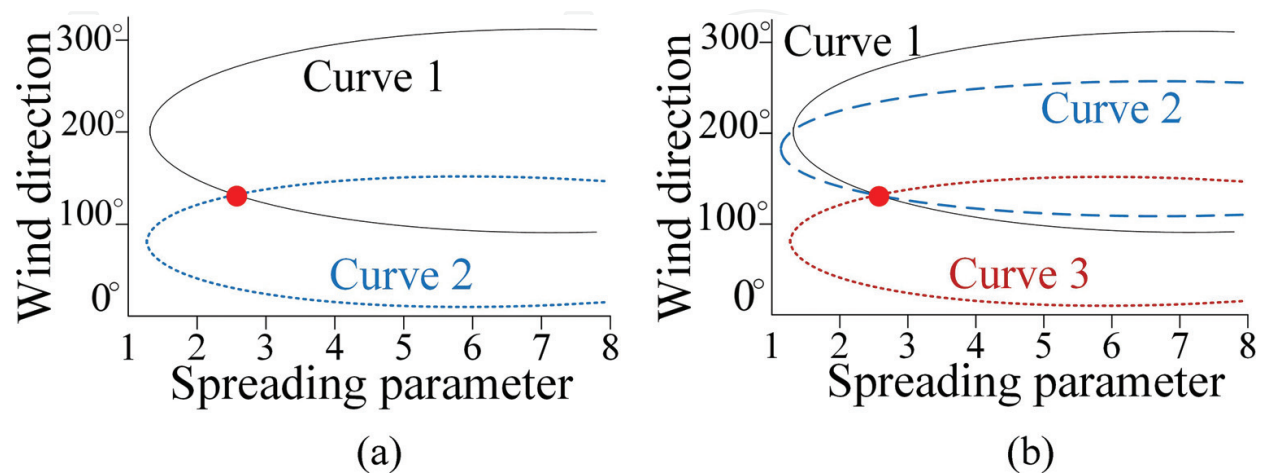

Figure 20. Relationship between the wind direction and the spreading parameter. (a) One-solution case. (b) Two-solution case.

$$s = \begin{cases} 0.2(\mu - 0.1)^{-1} & \mu > 0.1 \\ 2 & \mu < 0.1 \end{cases} \tag{26}$$

where $\mu = (C_D)^{1/2}(4\pi/g\lambda)^{1/2}U/\kappa$, $\kappa = 0.4$ is von Karman's constant and C_D is a drag coefficient proposed by Wu [19]

$$C_D = (0.8 + 0.065U) \times 10^{-3} \tag{27}$$

Substituting Eq. (27) into Eq. (26) and using the Cardano formula, we have

$$s = \begin{cases} 0.2\left(\frac{U}{\kappa}\sqrt{\frac{4\pi}{g\lambda}C_D} - 0.1\right)^{-1} & U > U^* \\ 2 & U < U^* \end{cases} \tag{28}$$

where U^* is related to the radar frequency.

When $U > U^*$, using the Cardano formula, we can derive the one-to-one correspondence relationship between U and s. Therefore, s can be considered as an indicator of U.

3.3.3. Simulation results

Simulation parameters: $f_0 = 5.283$ MHz, $v = 10$ knots, the true wind direction and speed are $\alpha_T^* = 90°$ and $U_T = 25$ knots, respectively. The true spreading parameter is $s_T \approx 2.1$ calculated by Eq. (28).

The relationship between the derived wind directions α^* and s is shown in **Figure 21a**. The solid curve indicates α^* versus s for the incident direction of $\phi_1 = 100°$, while the dashed curve represents the situation of the incident direction of $\phi_2 = 110°$. The intersection of these two curves determines a solution for α^* and s. Therefore, the extracted wind direction and the
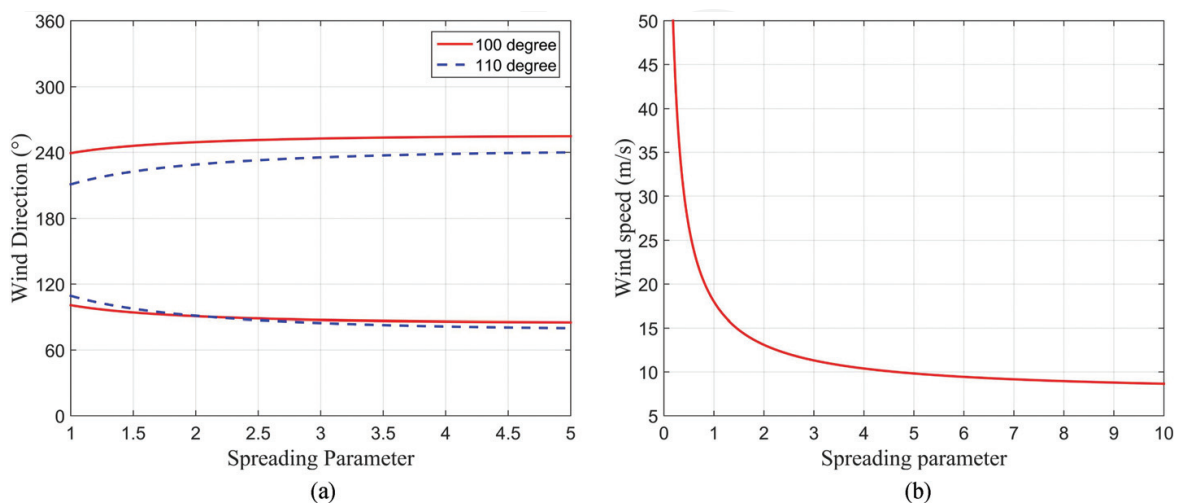

Figure 21. Deriving wind field. (a) Determination of α_E^* and s_E. (b) Determination of U.

spreading parameter are $\alpha_E^* \approx 90.02°$ and $s_E = 2.10$, respectively. The corresponding wind speed is $U_E \approx 24.98$ knots calculated by Eq. (28), as shown in **Figure 21b**.

3.3.4. Experimental results

The experimental data and the "real" wind field have been described in Section 3.2.4. **Figure 22** intuitively shows the radar-measured wind field distribution. From **Figure 22**, the majority of wind directions are north-northeast and north. Meanwhile, wind speeds gradually decrease and wind directions are slow-varying from north-northeast to north in the detection region from north to south. Therefore, the radar-measured results are in good agreement with the local wind field forecast.

Experimental results in Sections 3.2.4 and 3.3.4 show that the wind direction and field estimation in shipborne HFSWR have derived very encouraging results. However, there are some "bad points" that appear over the edge of the detection area, as shown in **Figures 17** and **22**, where a larger deviation exists. This may be because the effect of directional ambiguity is not totally eliminated due to the complex coastline structures. In addition, the ocean surface current, six oscillating motions of shipborne platform, and swell may be have negative effects on the wind direction and field estimations. Note that the method for wind field estimation is
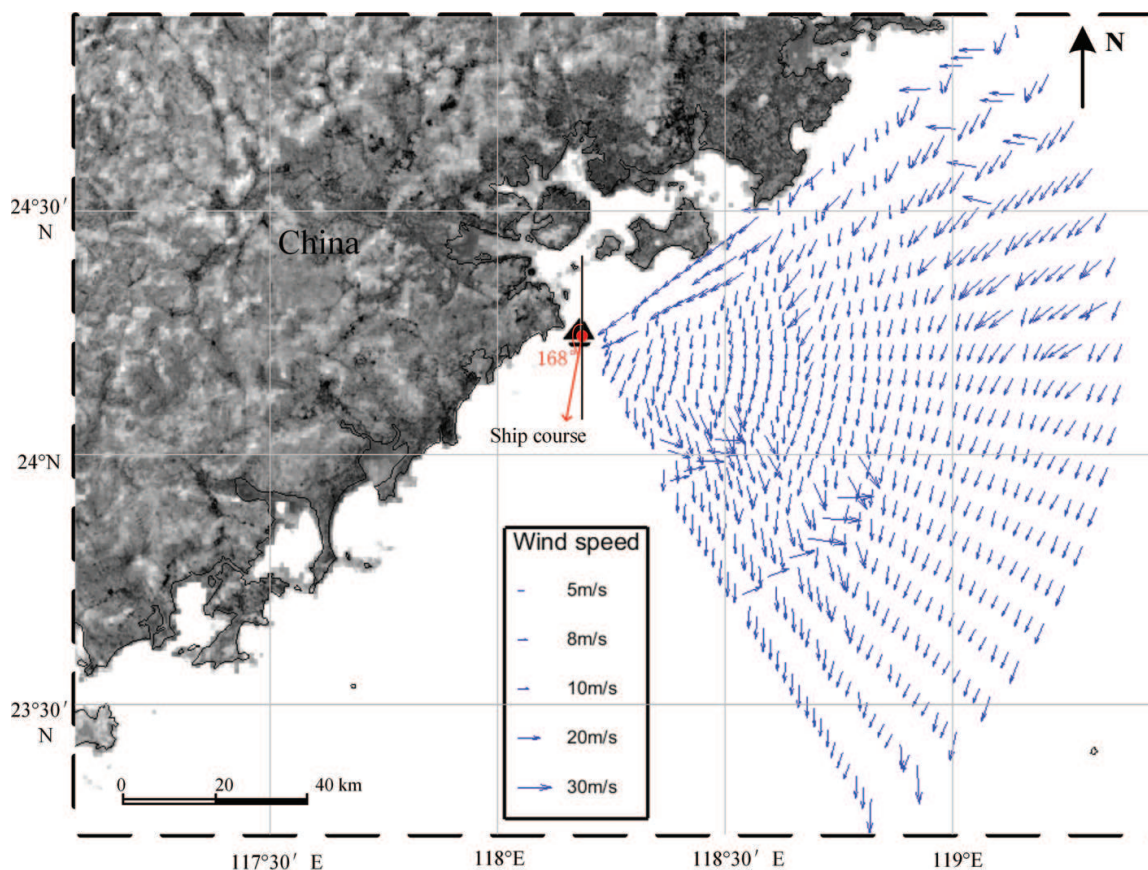

Figure 22. Wind direction map derived by shipborne HFSWR. The wind direction map is displayed with a range resolution interval each. Dot: Shipborne radar. Arrow: Ship course.

presented for a fully developed sea area and the wind speed inversion is conducted out only under the condition of $U > U^*$. Otherwise, the second-order spectra or other methods should be introduced. These are the subjects of ongoing investigations.

4. Remote sensing of ocean surface current with shipborne HFSWR

HFSWR system has been widely deployed for remote sensing of ocean surface current. With the development of signal-processing technology of HFSWR, shipborne HFSWR has gradually become a more potential deployment situation with its agility and maneuverability. Some experimental results and theoretical analyses have been conducted to explore the feasibility of remote sensing of ocean surface current in shipborne HFSWR [20–23]. In the previous works, however, the hull itself is either stationary or moving at a low speed without considering a high-speed case and effects of six DOFs motion on radar Doppler spectra. In this section, the potential of remote sensing of ocean surface radial current with shipborne HFSWR is presented [24]. Moreover, a stream function method is introduced to obtain current vector field using an improved music signal classification (MUSIC) algorithm and unitary transformation technique [25].

4.1. Remote sensing of ocean surface radial current

4.1.1. Received signal model

The shipborne platform exists six-DOF motion besides the forward movement owing to the effect of the complex ocean environment, which will introduce the superposed amplitude and phase modulations to the backscatter echoes [23], as shown in **Figure 23**. Considering antenna pattern, external noise, forward movement, and six-DOF motion, the time domain model of the received echo signal of the sea surface can be expressed as [25]
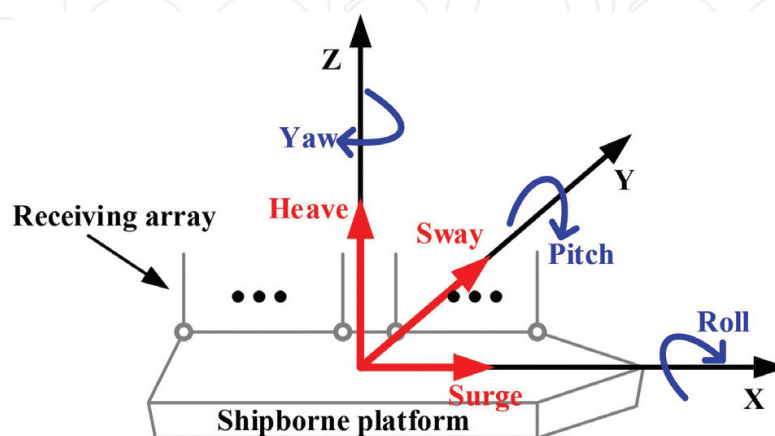

Figure 23. Diagram of six-DOF motion of shipborne platform.

$$x(R, t) = \sum_{r, s} \sigma(R_r, \theta_s, t) a(t) g(\theta_s, t) p(\theta_s, t) + e(t) \tag{29}$$

where $\sigma(R_r, \theta_s, t)$ is the first-order radar cross section of ocean surface, R_r and θ_s are the detection range and azimuth, respectively, $a(t)$ and $p(\theta_s, t)$ are the amplitude and phase of the array steering vector, respectively, $g(\theta_s, t)$ is the receiving antenna pattern, and $e(t)$ is the background noise.

4.1.2. Effect of six-DOF motion on ocean surface radial current estimation

In the previous section, a single antenna is used to estimate the directions of arrival (DOA) of sea echoes. In this case, however, the effects of ocean surface current are not considered. In order to estimate ocean surface radical current accurately, an antenna array with a high-resolution technique is necessary. Theoretical analyses [26] and experimental results [27] have demonstrated that MUSIC algorithm can achieve a good azimuthal resolution in ocean surface current estimation with short aperture. In this section, therefore, the MUSIC algorithm is employed to derive DOA.

From Section 2.1, the first-order Doppler spectra are spread due to the forward movement of shipborne HFSWR, and the spreading region increases with the increasing speed of the platform. That means the Bragg energies have been distributed into more peaks, and the spreading peaks exhibit many more Doppler sampling points which can be exploited to estimate DOA. From **Figure 24a**, the sampling points increase with the increasing platform speed. However, the performance of radial current estimation decreases. In particular, a higher RMSE appears when the ship is still, which may be because of lacking of sampling points. Meanwhile, the radial current RMSE is really high when the ship moves at a high speed, which may be caused by a low SNR. Therefore, the relationship between the RMSE and the platform speed would be a significant reference for the real sailing speed.
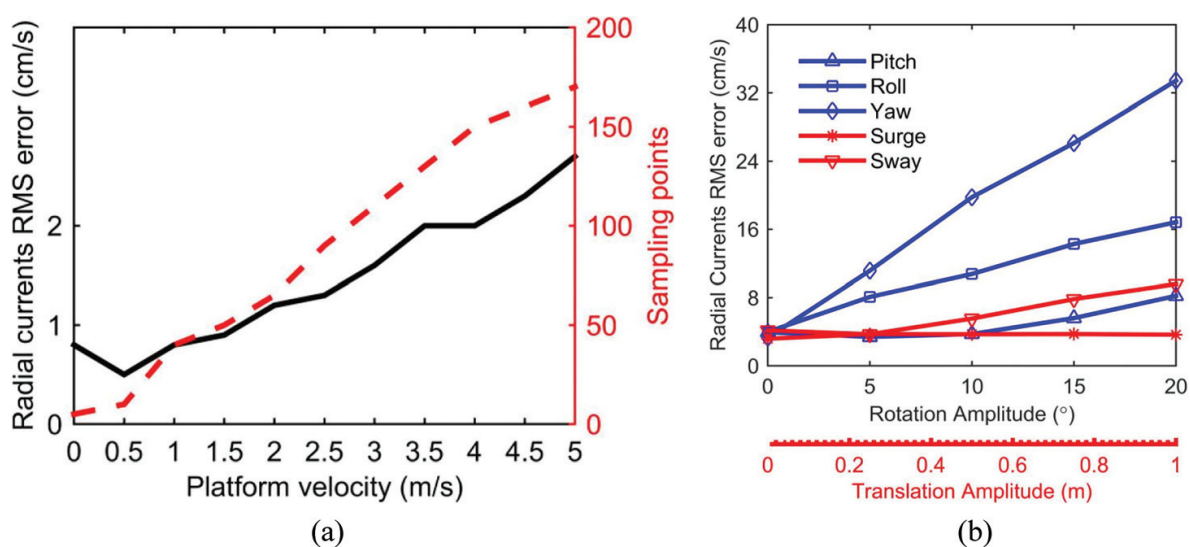

Figure 24. (a) Measurement errors of different platform speeds. (b) Effects of six-DOF motion.

From **Figure 24b**, the radial current RMSEs increase with the increasing amplitude of rotation (pitch, roll, and yaw) and sway. In particular, the surge has no severe influence on the measurement performance, which may be because the surge is generally in the direction of the platform-forward movement. Additionally, yaw plays the most important effect on the radial current estimation. Simulation results show the feasibility of remote sensing of ocean surface radial current in shipborne HFSWR. In addition, the performance of the current estimation is sensitive to the variation of amplitude of six-DOF motion besides surge, rather than the forward movement of the platform.

4.2. Remote sensing of ocean surface current vector field

4.2.1. Method for current vector measurement using RVSR-MUSIC

From Section 4.1, the estimate accuracy of DOA algorithm has significant influence on the performance of ocean surface current measurement. In order to take advantage of the limited radar data to improve the estimate accuracy of DOA, a real-valued MUSIC algorithm based on sparse-representing technique (RVSR-MUSIC) has been presented [25]. Once RVSR-MUSIC has been exploited to estimate DOA, the sea clutter spectra of shipborne HFSWR can be extracted with high resolution, and the Doppler frequency shift and the corresponding azimuth can be derived. Then, the radial velocity $\widehat{V}_r$ of ocean surface current at azimuth $\widehat{\phi}$ can be expressed as

$$\widehat{V}_r = \frac{\lambda}{2}\left(\frac{\widehat{f}_d \mp \sqrt{\frac{g}{\pi\lambda}} - 2v\cos\widehat{\phi}}{\lambda}\right) \tag{30}$$

where λ is the radiation wavelength, $\widehat{f}_d$ is the Doppler frequency shift, g is the gravitational acceleration, and $\widehat{\phi}$ is the corresponding azimuth.

As shown in **Figure 25**, the radial velocity of ocean surface current $V_r(x, y)$ in azimuth ϕ can be written as [25]

$$V_r(x, y) = \frac{xu(x, y) + yw(x, y)}{\sqrt{x^2 + y^2}} \tag{31}$$

According to the introduction of stream function in [28], we have [25]

$$V(x, y) = \sqrt{u^2(x, y) + w^2(x, y)} \tag{32}$$

$$\gamma(x, y) = \begin{cases} \tan^{-1}[w(x, y)/u(x, y)] & , \text{if } u(x, y) \geq 0 \\ \pi + \tan^{-1}[w(x, y)/u(x, y)], \text{else} \end{cases} \tag{33}$$

where $V(x, y)$ and $\gamma(x, y)$ are the amplitude and the direction of ocean surface current vector $\overrightarrow{V}(x, y)$, respectively.

4.2.2. Simulation results

Simulations are conducted under these conditions: the number of the receiving antenna is $M = 7$, the space between antennas is $d = \lambda/2$, the radar-operating frequency $f_0 = 7.5\,\text{MHz}$, the radar modulation period $T_r = 0.5\,\text{s}$, and the platform speed $v = 10\,\text{m/s}$ [25]. We assume a uniform ocean surface current field with a velocity of 0.5 m/s. Three different methods including spatial smoothing MUSIC (SS-MUSIC), complex-valued SR-MUSIC (CVSR-MUSIC), and RVSR-MUSIC are exploited to estimate ocean surface radial current by 50 independent Monte Carlo trials, as shown in **Figure 26**. It is obvious that RVSR-MUSIC is the most efficient algorithm for ocean surface radial current estimation.

Figure 27 shows the amplitude errors of the uniform current field using RVSR-MUSIC algorithm for radial current measurements and the second-order stream function for surface current vector measurements. It is apparent that a majority of amplitude errors are within 0.1 m/s. Simulation results demonstrate that the remote sensing of ocean surface current field using a single shipborne HFSWR is feasible. RVSR-MUSIC algorithm obtains the best estimation performance compared with other algorithms.
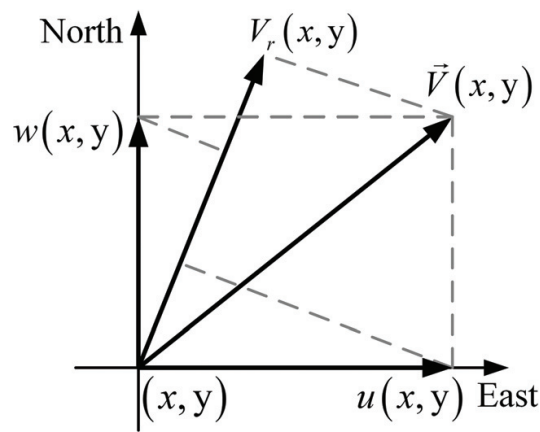

Figure 25. Geometrical relation between 2D surface current vector and radial current.
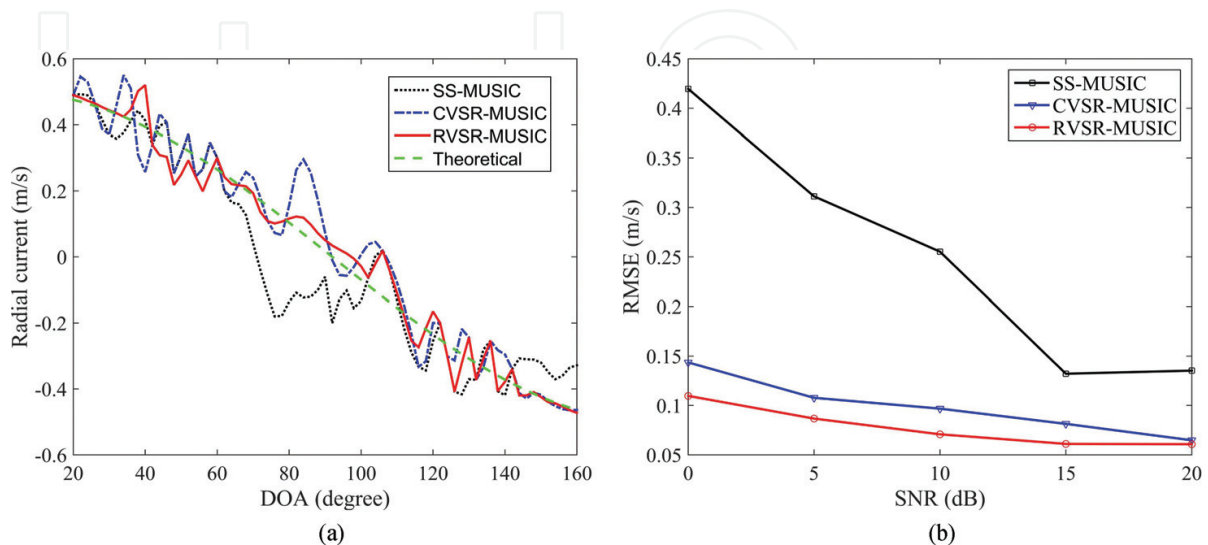

Figure 26. Performance estimation of ocean surface current. (a) Radial current profile. (b) RMSE of radial current versus SNR.
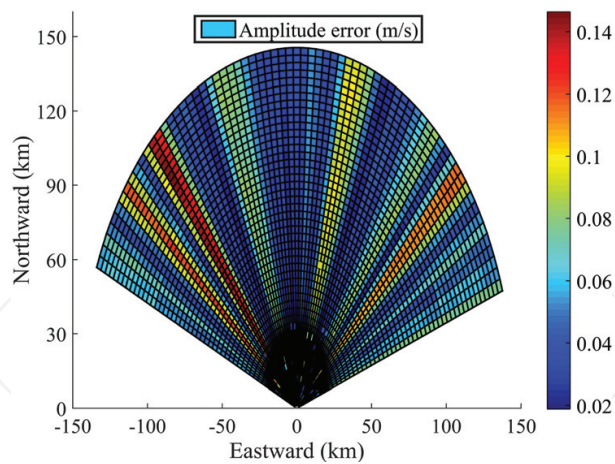
Figure 27. Estimated current field with RVSR-MUSIC.

Analyses of the simulation results show that the presented method here has derived very encouraging results. However, the effects of practical conditions in shipborne HFSWR should be considered. First, when HFSWR is mounted on a ship, the iron body distorts the electromagnetic field severely, which will lower azimuth resolution. Second, the nonideal motions will introduce a superposed amplitude and phase modulation to the backscatter echoes. Third, although RVSR-MUSIC algorithm can increase estimation accuracy and reduce the computational cost, unitary transformation is based on a centro-symmetrical array (CSA), which will severely limit the applications. In addition, the prerequisite of this method is that two-dimensional (2D) ocean surface current field is horizontally nondivergent (or incompressible). These are the subjects of ongoing investigations.

Author details

Junhao Xie[1]*, Minglei Sun[2], Zhenyuan Ji[1] and Guowei Yao[1]

*Address all correspondence to: xj@hit.edu.cn

1 Harbin Institute of Technology, Harbin, China

2 The 27th Research Institute of China Electronics Technology Group Corporation, Zhengzhou, China

References

[1] Xie J, Sun M, Ji Z. First-order ocean surface cross-section for shipborne HFSWR. Electronics Letters. 2013;**49**(16):1025-1026

[2] Sun M, Xie J, Ji Z, Cai W. Second-order ocean surface cross section for shipborne HFSWR. IEEE Antennas and Wireless Propagation Letters. 2015;**14**:823-826

[3] Sun M, Xie J, Ji Z, Yao G. Ocean surface cross sections for shipborne HFSWR with sway motion. Radio Science. 2016;**51**(11):1745-1757

[4] Walsh J, Huang W, Gill E. The first-order high frequency radar ocean surface cross section for an antenna on a floating platform. IEEE Transactions on Antennas and Propagation. 2010;**58**(9):2994-3003

[5] Lipa BJ, Barrick DE. Extraction of sea state from HF radar sea echo: Mathematical theory and modeling. Radio Science. 1986;**21**(1):81-100

[6] Shearman ED. HF ground-wave radar for sea-state and swell measurements: Theoretical studies, experiments and proposals. In: IEEE International Conference on Radar; London, United Kingdom. October 1982. pp. 101-106

[7] Xie J, Yuan Y, Liu Y. Experimental analysis of sea clutter in shipborne HFSWR. IEEE Proceedings-Radar, Sonar and Navigation. 2001;**148**(2):67-71

[8] Walsh J, Huang W, Gill E. The second-order high frequency radar ocean surface cross section for an antenna on a floating platform. IEEE Transactions on Antennas and Propagation. October 2012 **60**(10):4804-4813

[9] Barrick DE. First-order theory and analysis of MF/HF/VHF scatter from the sea. IEEE Transactions on Antennas and Propagation. 1972;**AP-20**(1):2-10

[10] Walsh J, Gill E. An analysis of the scattering of high-frequency electromagnetic radiation from rough surfaces with application to pulse radar operating in backscatter mode. Radio Science. 2000;**35**(6):1337-1359

[11] Sun M, Xie J, Ji Z, Cai W. Remote sensing of ocean surface wind direction with shipborne high frequency surface wave radar. In: IEEE Radar Conference on Radar; Arlington, VA, USA. May 2015. pp. 39-44

[12] Xie J, Yao G, Sun M, Ji Z, Li G, Geng J. Ocean surface wind direction inversion using shipborne high frequency surface wave radar. IEEE Geoscience and Remote Sensing Letters. 2017;**14**(8):1283-1287

[13] Huang W, Gill E, Wu S, Wen B, Yang Z, Hou J. Measuring surface wind direction by monostatic HF ground–wave radar at the eastern China Sea. IEEE Journal of Oceanic Engineering. October 2004;**29**(4):1032-1037

[14] Zhang J, Walsh J, Gill E. Inherent limitations in high-frequency radar remote sensing based on Bragg scattering from the ocean surface. IEEE Journal of Oceanic Engineering. July 2012;**37**(3):395-406

[15] Shen C, Gill E, Huang W. Extraction of swell parameters from simulated noisy HF radar signals. In: IEEE Radar Conference on Radar; Ottawa, Canada. April 2013. pp. 1-6

[16] Heron ML. Applying a unified directional wave spectrum to the remote sensing of wind wave directional spreading. Canadian Journal of Remote Sensing. 2002;**28**(3):246-353

[17] Heron ML, Prytz A. Wave height and wind direction from the HF coastal ocean surface radar. Canadian Journal of Remote Sensing. 2002;**28**(3):385-393

[18] Tayler GL, Teague CC, Stewart RH, Munk AM, Joy JW. Wave directional spectra from synthetic observations of radio scatter. Deep-Sea Research. 1974;**21**(12):989-1016

[19] Wu J. Wind-stress coefficients over sea surface from breeze to hurricane. Journal of Geophysical Research. 1982;**87**(C12):9704-9706

[20] Teague CC. Multifrequency HF radar observations of currents and current shears. IEEE Journal of Oceanic Engineering. April 1986;**OE-11**(2):258-269

[21] Lipa BJ, Barrick DE, Isaacson J, Lilleboe PM. CODAR wave measurements from a north sea semisubmersible. IEEE Journal of Oceanic Engineering. April 1990;**15**(2):119-125

[22] Gurgel KW. Experience with shipborne measurements of surface current fields by HF radar. Oceanography. 1997;**10**(2):82-84

[23] Gurgel KW, Essen H. On the performance of a shipborne current mapping HF radar. IEEE Journal of Oceanic Engineering. January 2000;**25**(1):183-191

[24] Chang G, Li M, Xie J, Zhang L, Yu C, Ji Y. Ocean surface current measurement using shipborne HF radar: Model and analysis. IEEE Journal of Oceanic Engineering. October 2016;**41**(4):970-981

[25] Wang Z, Xie J, Ji Z, Quan T. Remote sensing of surface currents with single shipborne high-frequency surface wave radar. Ocean Dynamics. 2016;**66**(1):27-39

[26] Laws KE, Fernandez DM, Paduan JD. Simulation-based evaluations of HF radar ocean current algorithms. IEEE Journal of Oceanic Engineering. October 2000;**25**(4):481-491

[27] Yang S, Ke H, Wu X, Tian J, Hou J. HF radar ocean current algorithm based on MUSIC and the validation experiments. IEEE Journal of Oceanic Engineering. July 2005;**30**(3):601-618

[28] Liu L, Wu X, Cheng F, Yang S, Ke H. Algorithm for HF radar vector current measurements. Journal of Geophysical Research. 2007;**63**(1):47-66